

# EVOLUTION OF THE RADIUS VALLEY AROUND LOW MASS DWARF STARS WITH *KEPLER* AND *K2*

RYAN CLOUTIER<sup>1,2</sup>

*Draft version October 10, 2019*

## ABSTRACT

Recent observational studies have revealed a prominent gap in the occurrence rate of close-in planet radii around Sun-like stars. Resolving the so-called radius valley around low mass stars can provide valuable constraints on the physical mechanisms that sculpt the valley and so far have been largely limited by relatively poor counting statistics. Here we calculate the occurrence rate of small close-in planets around low mass dwarf stars using the known planet populations from both the primary *Kepler* and *K2* missions while exploiting the precise *Gaia* DR2 data to refine the stellar radii and masses. After applying appropriate completeness corrections to the empirical planet populations, the radius valley is clearly resolved in the maximum a-posteriori occurrence rates although the gap is not completely void of planets, a feature whose prominence increases with decreasing stellar mass. We also show that the location of valley features evolve to smaller planet sizes with decreasing stellar mass in agreement with competing models of photoevaporation and core-powered mass loss. Although current measurements are insufficient to firmly distinguish either model as the dominant formation pathway of the radius valley, we argue that robust inferences will require  $\mathcal{O}(\mathbf{N})$  additional confirmed close-in planets around low mass stars which are expected to be uncovered by *TESS* within its extended mission.

## 1. INTRODUCTION

NASA’s *Kepler* space telescope has discovered thousands of exoplanets over its lifetime and consequently enabled robust investigations of the occurrence rate of planets within our galaxy. One striking outcome of such studies was that the so-called super-Earths and sub-Neptunes—whose radii span sizes intermediate between those of the Earth and Neptune—represent the most common type of planet around Sun-like stars and early M dwarfs alike (e.g. Youdin 2011; Howard et al. 2012; Dressing & Charbonneau 2013; Fressin et al. 2013; Petigura et al. 2013; Morton & Swift 2014; Dressing & Charbonneau 2015; Gaidos et al. 2016; Fulton et al. 2017; Hardegree-Ullman et al. 2019). Furthermore, mass measurements of many of these transiting planets via transit-timing variations or precision radial velocity follow-up campaigns revealed that the majority of planets smaller than  $\sim 1.6 R_{\oplus}$  are consistent with having bulk terrestrial compositions (e.g. Weiss & Marcy 2014; Dressing et al. 2015; Rogers 2015). Early studies of the *Kepler* planet population hinted at the distribution of planet radii at small orbital separations featuring a bimodality (e.g. Owen & Wu 2013)—commonly referred to as the radius valley—that is thought to depict a population of small, predominantly rocky super-Earths plus a population of inflated sub-Neptunes that have retained significant H/He envelopes.

Consequently, numerous studies of planet formation and evolution sought to explain the apparent bimodality in the distribution of close-in planetary radii. One such proposed mechanism is that of photoevaporation wherein the gaseous envelopes of small close-in planets may be stripped by X-ray and extreme ultraviolet (XUV) radia-

tion from their host stars during the first  $\sim 100$  Myrs of the planet’s lifetime (Owen & Wu 2013; Jin et al. 2014; Lopez & Fortney 2014; Chen & Rogers 2016; Lopez & Rice 2018; Owen & Wu 2017; Jin & Mordasini 2018). Another possible explanation invokes gas-poor formation wherein gas accretion is delayed by dynamical friction whilst the protoplanet is still embedded within the protoplanetary disk until a point at which the gaseous disk has almost completely dissipated after just a few Myrs (Lee et al. 2014; Lee & Chiang 2016; Lopez & Rice 2018). More recently, the radius valley may also be explained by core-powered mass loss wherein the luminosity from a planetary core’s primordial energy reservoir from formation drives atmospheric escape over Gyr timescales (Ginzburg et al. 2018; Gupta & Schlichting 2019a,b).

Observational tests of the aforementioned theoretical frameworks have become feasible in recent years as a result of the precise refinement of measured planet radii following improved stellar host characterization via spectroscopy, asteroseismology, and *Gaia* parallaxes (e.g. Fulton et al. 2017; Van Eylen et al. 2018; Fulton & Petigura 2018; Martinez et al. 2019). These studies clearly resolved the radius valley among small close-in planets around Sun-like stars. They also observed a variety of trends in either the raw or in the completeness-corrected (i.e. the occurrence rate) distributions of close-in planets. Firstly, the location of the radius valley around FGK stars is period-dependent with slope  $d \log r_p / d \log P \sim -0.1$  (Van Eylen et al. 2018; Martinez et al. 2019), a result that is consistent with both photoevaporation and core-powered mass loss models but is inconsistent with the late formation of terrestrial planets in a gas-poor environment. Secondly, the feature locations (i.e. the weighted average radius of the peaks and valley) appear to exist at smaller planet radii with decreasing stellar mass (Fulton & Petigura 2018; Wu 2019).

In this study, we extend the investigation of the occurrence rate of close-in planets to systems hosted by

cloutier@cfa.harvard.edu

<sup>1</sup> Center for Astrophysics | Harvard & Smithsonian, 60 Garden Street, Cambridge, MA, 02138, USA

<sup>2</sup> Dept. of Astronomy & Astrophysics, University of Toronto, 50 St. George Street, Toronto, ON, M5S 3H4, Canada

FIG. 1.— Empirical distributions of *Kepler* planet radii. Histograms of *Kepler* planet radii from Berger et al. (2018) for planets with host stellar effective temperatures  $T_{\text{eff}} \in [4700, 6500]$  K (blue) and  $T_{\text{eff}} < 4700$  K (red). The former subset of 2816 planets corresponds to the effective temperature range considered in the CKS (Fulton et al. 2017) wherein the radius valley is clearly resolved in the empirical distribution even without completeness corrections. A similar bimodal structure is not resolved in the empirical distribution of the latter subset around cool stars due in-part to the relatively poor counting statistics with just 350 planets.

low mass dwarf stars later than mid-K dwarfs. The known planet population in this stellar mass regime features nearly an order of magnitude fewer planets than around Sun-like stars, thus making the detection of the radius valley around low mass stars more difficult and at a lower signal-to-noise. This fact is clearly evidenced in the empirical *Kepler* planet population for which the radius valley around Sun-like stars ( $T_{\text{eff}} \in [4700, 6500]$  K) is clearly exhibited whereas any valley in the planet population around low mass stars ( $T_{\text{eff}} < 4700$  K) is not easily discernible by-eye (see Fig. 1 based on the data from Berger et al. 2018). Our study leverages the precise stellar parallaxes from the *Gaia* DR2 for low mass stars observed by *Kepler* and *K2* to refine the stellar parameters and compute precise occurrence rates of close-in planets with the goal of resolving the radius valley and accurately measuring the locations of the radius valley features and their uncertainties. Although it is unlikely that a single physical mechanism is responsible for sculpting the radius valley, investigation the evolution of the valley features with stellar mass can allude to which process—if any—dominates the evolution of close-in planets.

In Sect. 2 we define our stellar sample from *Kepler* and *K2*. In Sect. 3 we compile our sample of confirmed planets which we supplement with a suite of *K2* planet candidates to improve the counting statistics. In Sect. 4 we derive the transiting planet detection completeness from each mission and use those results to calculate the occurrence rate of small close-in planets and resolve the radius valley in Sect. 5. Our results as a function stellar mass are compared to predictions from models of photo-evaporation and core-powered mass loss in Sect. 6. We conclude with a discussion of our results and its implications in Sect. 7.

## 2. LOW MASS DWARF STELLAR SAMPLE

The goal of this study is to extend measurements of the radius valley and its properties to planetary systems hosted by low mass dwarf stars with effective temperatures  $T_{\text{eff}} < 4700$  K: the lower limit of  $T_{\text{eff}}$  considered by Fulton & Petigura (2018). This adopted temperature threshold approximately corresponds to spectral types later than K3.5V (Pecaut & Mamajek 2013). In the following subsections we define our stellar sample from both *Kepler* or *K2*.

### 2.1. *Kepler* Stellar Sample

Following the release of *Gaia* DR2 (Lindgren et al. 2018), Berger et al. (2018) cross-matched *Kepler* target stars with DR2 and compiled a catalog of stellar parallaxes  $\varpi$ , 2MASS  $K_s$ -band magnitudes, and spectroscopic measurements of  $T_{\text{eff}}$ ,  $\log g$ , and  $[\text{Fe}/\text{H}]$  for  $\sim 178,000$  stars observed as part of the primary *Kepler* mission. Spectroscopic measurements were obtained from either the DR25 *Kepler* Stellar Properties Catalog

(KSPC; Mathur et al. 2017), the California Kepler Survey (CKS; Petigura et al. 2017) where available, and  $T_{\text{eff}}$  values for stars with  $T_{\text{eff}} < 4000$  K were compiled from Gaidos et al. (2016). The full set of available stellar parameters are used as input within the spectral classification code *isoclassify* (Huber et al. 2017) to calculate stellar luminosities. The resulting luminosity values were consequently combined with the  $T_{\text{eff}}$  measurements to refine the stellar radii using the Stefan-Boltzmann law for the majority of *Kepler* FGK stars. However, bolometric corrections for *Kepler* M dwarfs with  $T_{\text{eff}} < 4100$  K and absolute  $K_s$ -band magnitudes  $M_{K_s} > 3$  are known to suffer significant inaccuracies owing to incomplete molecular line lists. For these stars, Berger et al. (2018) instead adopted the empirically-derived M dwarf radius-luminosity relation from Mann et al. (2015) to refine their M dwarf stellar radii. Berger et al. (2018) also used the  $T_{\text{eff}}$  values and their luminosity measurements to derive stellar evolutionary flags that classify their stars as either a dwarf, a subgiant, or a red giant.

Stellar masses  $M_s$  are not reported by Berger et al. (2018). In order to study the *Kepler* planet population as a function of  $M_s$ , we derive  $M_s$  values given the measured stellar radii  $R_s$  using the mass-radius relation from Boyajian et al. (2012) which is applicable to both K and M dwarfs. Boyajian et al. (2012) acquired interferometric measurements with the *CHARA* array of 21 nearby K and M dwarfs to measure the angular size of each stellar disk at the level of  $\lesssim 5\%$ . Their stellar sample was supplemented by 12 literature measurements of  $R_s$  from interferometry. Mass measurements were then derived using the  $K_s$ -band mass-luminosity relation from Henry & McCarthy (1993) which was valid for their full stellar sample spanning  $0.13\text{--}0.90 R_{\odot}$ . Boyajian et al. (2012) parameterized the stellar mass-radius relationship as a quadratic in  $M_s$  and reported values and uncertainties for each polynomial coefficient. Here, we assume independent Gaussian probability density functions (PDF) for each coefficient and sample their values along with each star's  $R_s$  from their respective measurement uncertainties to derive the  $M_s$  PDF for all of the low mass dwarfs in our *Kepler* sample.

We define our final *Kepler* stellar sample by focusing on stars that satisfy the following criteria:

1. *Kepler* magnitude  $K_p < 16$ ,
2.  $T_{\text{eff}} - \sigma_{T_{\text{eff}}} \leq 4700$  K,
3.  $R_s - \sigma_{R_s} \leq 0.8 R_{\odot}$ ,
4.  $M_s - \sigma_{M_s} \leq 0.8 M_{\odot}$ , and
5. and an evolutionary flag corresponding to a dwarf star.

Based on these criteria, we retrieve 3965 low mass *Kepler* stars whose stellar parameters are depicted in Fig. 2. In our *Kepler* sample, the *Kepler* magnitudes span  $K_p \in [10.35, 16.00]$  with a median value of 15.16, effective temperatures span  $T_{\text{eff}} \in [3154, 4870]$  K with a median value of 4394 K, stellar radii span  $R_s \in [0.17, 0.87] R_{\odot}$  with a median value of  $0.68 R_{\odot}$ , and stellar masses span  $M_s \in [0.13, 0.88] M_{\odot}$  with a median value of  $0.70 M_{\odot}$ . The stars in this sample exhibit a median fractional  $R_s$

uncertainty of  $\sim 6.7\%$  which is  $\sim 4 - 5$  times smaller than the typical  $R_s$  uncertainty reported in the KSPC. The median fractional uncertainty on  $M_s$  is  $\sim 5.5\%$ .

## 2.2. *K2* Stellar Sample

We first retrieved the list of probable low mass dwarf stars observed in any *K2* campaign by querying MAST<sup>3</sup>. Our initial search was restricted to *K2* stars with  $T_{\text{eff}} < 4900$  K,  $\log g > 4$ , and  $R_s < 1 R_\odot$ . Note that these criteria are not intended to represent the parameter ranges for low mass dwarf stars but are intended as conservative conditions to encapsulate all such stars prior to their refinement based on the *Gaia* DR2 data. From MAST we retrieve each star’s Ecliptic Plane Input Catalog (EPIC) numerical identifier, stellar photometry in the *Kepler* bandpass  $K_p$  and 2MASS bands  $JHK_s$ , along with measured values of  $T_{\text{eff}}$ ,  $\log g$ ,  $[\text{Fe}/\text{H}]$ , and  $R_s$ .

We proceed with refining the stellar parameters by cross-matching our initial *K2* sample with *Gaia* DR2 using the *Gaia-K2* data products from Megan Bedell<sup>4</sup>. Where available, we retrieve each star’s celestial coordinates, stellar parallaxes  $\varpi$ , and *Gaia* photometry. Measurements of  $R_s$  then follow from the methodology outlined in Berger et al. (2018). The formalism of Bailer-Jones et al. (2018) is used to transform the assumed Gaussian-distributed  $\varpi$  PDFs into stellar distance PDFs which need not remain Gaussian. Using the measured distances  $d$  and celestial coordinates, we interpolate over the  $E_{B-V}$  extinction maps using the `mw dust` software (Bovy et al. 2016) to derive both the  $V$  and  $K_s$ -band extinction coefficients  $A_V$  and  $A_{K_s}$ . We then calculate each star’s absolute  $K_s$ -band magnitude  $M_{K_s} = K_s - \mu - A_{K_s}$  where the distance modulus is  $\mu = 5 \log_{10}(d/10 \text{ pc})$ .

For the earliest stars in our sample ( $M_{K_s} \leq 4.6$ ), for which the bolometric corrections are still reliable, we interpolate the MIST bolometric correction grids (Choi et al. 2016) over  $T_{\text{eff}}$ ,  $\log g$ ,  $[\text{Fe}/\text{H}]$ , and  $A_V$  to derive the  $K_s$ -band bolometric corrections  $BC_{K_s}$ . We then compute the absolute bolometric magnitude  $M_{\text{bol}} = M_{K_s} + BC_{K_s}$  and consequently the bolometric stellar luminosities as

$$L_{\text{bol}} = L_0 \cdot 10^{-0.4M_{\text{bol}}}, \quad (1)$$

where  $L_0 = 3.0128 \times 10^{28}$  W (Mamajek et al. 2015). The refined  $R_s$  values are then calculated using the Stefan-Boltzmann law given  $L_{\text{bol}}$  and  $T_{\text{eff}}$  with measurement uncertainties propagated throughout.

For the remaining late type stars with  $M_{K_s} > 4.6$ , we revert to the empirically-derived radius-luminosity relation from Mann et al. (2015) to calculate the M dwarf stellar radii. Mann et al. (2015) fit a second-order polynomial to  $R_s$  as a function of  $M_{K_s}$  which has a characteristic dispersion in the fractional radius uncertainty of 2.89%. To quantify the final  $R_s$  uncertainty we sample  $M_{K_s}$  from its posterior PDF and transform each  $M_{K_s}$  draw to an  $R_s$  value using the aforementioned radius-luminosity relation. To each star’s derived  $R_s$  PDF, we

FIG. 2.— Low mass dwarf stellar samples from *Kepler* and *K2*. Distributions of *Kepler* magnitudes, effective temperatures, stellar radii, and stellar masses for stars in our final stellar sample from either *Kepler* (blue histogram and markers) or *K2* (red histogram and markers).

add in quadrature an additional dispersion term whose fractional uncertainty is 2.89%. Stellar masses within our *K2* sample are derived identically to the method applied to the *Kepler* sample (see Sect. 2.1) using the Boyajian et al. (2012) stellar mass-radius relation.

We define our final *K2* stellar sample of low mass dwarf stars similarly to our definition of the *Kepler* sample. Explicitly, we focus on stars that obey the following criteria:

1.  $K_p < 14.7$ ,
2.  $T_{\text{eff}} - \sigma_{T_{\text{eff}}} \leq 4700$  K,
3.  $R_s - \sigma_{R_s} \leq 0.8 R_\odot$ ,
4.  $M_s - \sigma_{M_s} \leq 0.8 M_\odot$ , and
5.  $R_s < R_{s,\text{max}}$ .

Because our *K2* sample lacks any evolutionary flags, we adopt the following ad hoc upper limit on  $R_s$  from Fulton et al. (2017) that aims to reject evolved stars:

$$R_{s,\text{max}} = R_\odot \cdot 10^{0.00025(T_{\text{eff}}/\text{K} - 5500) + 0.2}. \quad (2)$$

Based on these criteria, we retrieve 13428 low mass *K2* stars whose stellar parameters are also depicted in Fig. 2. In our *K2* sample, the *Kepler* magnitudes span  $K_p \in [8.47, 14.68]$  with a median value of 14.04, effective temperatures span  $T_{\text{eff}} \in [3246, 4856]$  K with a median value of 4017 K, stellar radii span  $R_s \in [0.14, 0.94] R_\odot$  with a median value of  $0.70 R_\odot$ , and stellar masses span  $M_s \in [0.09, 0.93] M_\odot$  with a median value of  $0.69 M_\odot$ . The stars in this sample exhibit a median fractional  $R_s$  uncertainty of  $\sim 3.5\%$  which is  $\sim 2$  times smaller than the typical  $R_s$  uncertainty obtained for stars in our *Kepler* sample. The median fractional uncertainty on  $M_s$  is  $\sim 3.9\%$ .

## 3. POPULATION OF SMALL CLOSE-IN PLANETS AROUND LOW MASS DWARF STARS

Here we define the population of small close-in planets orbiting stars contained in our stellar sample. Our initial sample of transiting planets from either *Kepler* or *K2* were retrieved from the NASA Exoplanet Archive (Akeson et al. 2013) on June 15, 2019. Only confirmed planets—based on their Exoplanet Archive dispositions—with orbital periods  $P \in [0.5, 100]$  days are included. By considering confirmed planets only we naturally focus on a subset of the true empirical population of small close-in planets without being contaminated by various astrophysical false positive scenarios that may plague the planet candidates that are excluded from our initial sample.

The refined stellar radii derived in Sect. 2 enable us to derive more accurate and precise planetary radii. We refine the planetary radii  $r_p$  by retrieving point estimates of each planet’s scaled planetary radius  $r_p/R_s$  which often include a median value accompanied by the 16<sup>th</sup> and 84<sup>th</sup> percentiles. In cases for which the  $r_p/R_s$  uncertainties are symmetric, we assume that the  $r_p/R_s$  posterior

<sup>3</sup> Mikulski Archive for Space Telescopes, <https://archive.stsci.edu/k2/>.

<sup>4</sup> <https://gaia-kepler.fun/>



PDF is Gaussian. For planets with asymmetric reported uncertainties, we fit the  $r_p/R_s$  percentiles with a skew-normal distribution using the `scipy.skewnorm` python class. We fit for the location, scale, and shape parameters of the skew-normal distribution such that its resulting percentiles are consistent with the  $r_p/R_s$  point estimates reported for each planet. The refined planetary radii are then derived by sampling the fitted  $r_p/R_s$  and  $R_s$  distributions. Based on the refined  $r_p$  values we update our planet sample by only focusing on planets whose radii are consistent with  $0.5\text{--}4 R_\oplus$ .

From the distributions of  $R_s$ ,  $T_{\text{eff}}$ ,  $M_s$ , and  $P$  for each planet and host star, we derive the planets' semimajor axes  $a$  and insolation  $F$  via

$$\frac{F}{F_\oplus} = \left(\frac{R_s}{R_\odot}\right)^2 \left(\frac{T_{\text{eff}}}{5777 \text{ K}}\right)^4 \left(\frac{a}{1 \text{ AU}}\right)^{-2}. \quad (3)$$

Our final sample of confirmed small close-in planets contains 275 *Kepler* and 53 *K2* planets respectively. Their respective median fractional radius uncertainties are 7.1% and 9.0%. Planet properties of the 326 confirmed planets in our sample are reported in Tables 1 and 2. Our planet sample is depicted in Fig. 3 as two-dimensional maps of the number of planet detections in the period-radius and insolation-radius spaces. The two-dimensional histogram maps are computed by Monte-Carlo sampling planets from their  $F$  and  $r_p$  measurement uncertainties and with a fractional precision on  $P$  inflated to 20%.

#### 4. TRANSITING PLANET DETECTION COMPLETENESS

Derivation of the planet occurrence rate requires the empirical distribution of planet detections to be corrected for imperfect survey completeness. The completeness correction is treated separately for each subset of planets from *Kepler* or *K2* in the following subsections. Each set of corrections accounts for detection biases arising from the imperfect detection sensitivity and for the geometric probability of a planetary transit to occur.

##### 4.1. *Kepler* Sensitivity

The derivation of the *Kepler* planet detection sensitivity follows from the methodology outlined in Christiansen et al. (2016) and used by Fulton et al. (2017) to resolve the radius valley around FGK stars. Per-target *Kepler* completeness products for DR25 and the SOC 9.3 version of the *Kepler* pipeline (Jenkins et al. 2010) are available for all of the planet-host stars in our *Kepler* sample (Burke et al. 2015; Burke & Catanzarite 2017). Detection sensitivities (or efficiencies) were calculated via transiting planetary signal injections at the pixel level (Christiansen et al. 2015, 2017) which are subsequently processed by the *Kepler* pipeline's transiting planet search (TPS) module from which the detection sensitivity as a function of the Multi-event statistic (MES) is computed as the fraction of injected signals that are successfully recovered by the pipeline.

The MES represents the level of significance of a transit signal at a specified transit duration ranging from 1.5–15 hours. Following Petigura et al. (2018) we adopt an alternative diagnostic for the transit signal significance

in the form of the transit S/N

$$\text{S/N} = \frac{Z}{\text{CDPP}_D} \sqrt{n_{\text{transits}}(\mathbf{t}, P, T_0)} \quad (4)$$

where  $Z = (r_p/R_s)^2$  is the transit depth assuming a non-grazing transit (i.e.  $b \lesssim 0.9$ ),  $\text{CDPP}_D$  is the Combined Differential Photometric Precision on the timescale of the transit duration  $D$ , and  $n_{\text{transits}}$  is the number of observed transits given the target's data span and duty cycle<sup>5</sup> of observations  $\mathbf{t}$ , the planet's orbital period  $P$ , and its time of mid-transit  $T_0$ .

To compute the *Kepler* detection sensitivity as a function of S/N, we first derive the mapping between the MES and the transit S/N using the data from Christiansen et al. (2015) who derived the detection sensitivity of the *Kepler* pipeline from one year of data. The parameters of the injected planets are provided along with their corresponding MES and CDPP at each value of  $D$  considered. For each injected planet we interpolate its MES and CDPP values to  $D$  and calculate the transit S/N using Eq. 4. The mapping between MES and S/N is shown in Fig. 4 for the full set of injected planets whose transit S/N values span 2.7–4843. Given the large number of injected planetary signals ( $> 10^4$ ), we fit the number-weighted S/N to MES mapping using the `scipy.curve_fit` non-linear least squares algorithm with a powerlaw function of the form  $\text{MES} = A \cdot \text{S/N}^\alpha$ . We find a best-fit amplitude and powerlaw index of  $A = 0.977$  and  $\alpha = 0.967$  respectively with negligible uncertainties. This relation is used to map the transit S/N to MES which is then mapped to the detection sensitivity. The average *Kepler* detection sensitivity curve as a function of transit S/N, along with the 16<sup>th</sup> and 84<sup>th</sup> percentiles for the stars in our *Kepler* sample are shown in Fig. 5.

##### 4.2. *K2* Sensitivity

Unlike the primary *Kepler* mission, the *K2* data products do not feature detailed completeness and reliability products. To derive the detection sensitivity among the *K2* stars in our sample we employ the transit detection pipeline ORION (Cloutier 2019). The failure of the second reaction wheel onboard the *Kepler* spacecraft in 2013 prevented the observatory from maintaining the fine pointing accuracy required to obtain ultra precise photometry. The re-purposed *K2* mission exploited the solar wind pressure by enabling the observatory to continue pointing along the ecliptic plane with realignments via thrusters firings **every**  $\sim 6$  hours (Howell et al. 2014). ORION lacks a module to correct for the temporally correlated pointing corrections so as input we feed the EVEREST light curves which use a pixel level decorrelation to remove systematics from the spacecraft's variable pointing (Luger et al. 2016, 2018). We favor the EVEREST *K2* light curves over light curves produced by similar pipelines (e.g. K2SFF; Vanderburg & Johnson 2014, K2SC; Aigrain et al. 2015, 2016) due to its performance in obtaining improved photometric precision at the level of  $\sim 20\text{--}50\%$  (Luger et al. 2016).

We quantify the *K2* detection sensitivity using ORION by first retrieving the EVEREST light curve from MAST

<sup>5</sup> Number of useful cadences for transit signal detection.

FIG. 3.— Empirical population of confirmed close-in planets around low mass stars. The distribution of 275 and 53 confirmed planets from *Kepler* and *K2* respectively as a function of orbital period, insolation, and planet radius. The two-dimensional maps are Monte-Carlo sampled from the measurement uncertainties on the planetary radii and insolations while the fractional uncertainties on the orbital periods are inflated to 20%.

TABLE 1  
*Kepler* CONFIRMED PLANET PARAMETERS

KIC	Planet name	$P$ [days]	$F$ [ $F_{\oplus}$ ]	$F$ upper limit [ $F_{\oplus}$ ]	$F$ lower limit [ $F_{\oplus}$ ]	$r_p$ [ $R_{\oplus}$ ]	$r_p$ upper limit [ $R_{\oplus}$ ]	$r_p$ lower limit [ $R_{\oplus}$ ]
1873513	Kepler-1624 b	3.29030	36.3	5.9	5.5	6.53	0.19	0.20
2556650	Kepler-1124 b	2.85235	47.4	5.0	4.6	1.97	0.08	0.10
2715135	Kepler-753 b	5.74771	41.3	5.1	4.8	1.89	0.30	0.12
3234598	Kepler-383 b	12.90468	20.6	3.2	2.5	1.54	0.30	0.17
3234598	Kepler-383 c	31.20122	6.4	0.9	0.7	1.49	0.34	0.22

TABLE 2  
*K2* CONFIRMED PLANET PARAMETERS

EPIC	Planet name	$P$ [days]	$F$ [ $F_{\oplus}$ ]	$F$ upper limit [ $F_{\oplus}$ ]	$F$ lower limit [ $F_{\oplus}$ ]	$r_p$ [ $R_{\oplus}$ ]	$r_p$ upper limit [ $R_{\oplus}$ ]	$r_p$ lower limit [ $R_{\oplus}$ ]
201110617	K2-156 b	0.81315	1146.7	5038.8	734.4	1.35	0.12	0.10
201155177	K2-42 b	6.68796	93.9	353.9	58.8	2.45	0.27	0.25
201205469	K2-43 b	3.47114	83.9	316.0	52.2	4.09	0.28	0.25
201208431	K2-4 b	10.00440	34.2	167.1	23.5	2.52	0.34	0.31
201338508	K2-5 b	5.73597	47.3	209.2	29.5	1.95	0.17	0.18

FIG. 4.— Correlation between the *Kepler* multi-event statistic and transit S/N. The mapping between the MES and S/N based on the synthetic planetary signals injected into the *Kepler* pipeline (Christiansen et al. 2015). The number-weighted powerlaw fit (solid line) to the correlation differs slightly from a one-to-one relation (dashed line) with the.

FIG. 5.— Average detection sensitivity for *Kepler* and *K2*. The solid curves represent the average transiting planet detection sensitivity for the *Kepler* and *K2* stars in our sample as a function of the transit S/N (Eq. 4). The shaded regions mark the 16<sup>th</sup> and 84<sup>th</sup> percentiles of the measured detection sensitivities.

for each star in our sample. We only consider light curves from individual campaigns. As ORION input we supply the time sampling  $\mathbf{t}$  in BJD, the corrected flux, and flux uncertainties in  $e^-/\text{second}$ , from the EVEREST keywords TIME, FCOR, and FRAW\_ERR. The duty cycle is derived by restricting ourselves to light curve measurements for which the QUALITY flag is zero. Any known signals from planets, PCs, or FPs are removed from the light curve based on their reported transit parameters using the batman (Kreidberg 2015) implementation of the Mandel & Agol (2002) transit model. We then inject transiting planetary signals directly into the light curve by sampling planets from the linear transit S/N grid  $\mathcal{U}(0, 50)$ . The per-system multiplicity is drawn from the cumulative occurrence rate of small planets out to 200 days around mid-K to early M dwarfs from *Kepler* ( $2.5 \pm 0.2$ ; Dressing & Charbonneau 2015). Each planet’s time of mid-transit  $T_0$  is drawn from  $\mathcal{U}(\min(\mathbf{t}), \max(\mathbf{t}))$ . In a given light curve, with a fixed CDPP( $D$ ) and  $\mathbf{t}$ , for a star whose radius and mass are fixed to their maximum likelihood values, we draw each planet’s logarithmic orbital period from  $\mathcal{U}(\log_{10}(0.5 \text{ days}), \log_{10}(200 \text{ days}))$  which allows us to compute the number of transits that occur within  $\mathbf{t}$ . Note that some injected planets will exhibit  $n_{\text{transits}} = 0$

due to the limited *K2* baselines of typically  $\sim 80$  days. The drawn orbital period also uniquely determines the planet’s radius corresponding to its drawn value of the S/N. To ensure dynamical stability in multi-planet systems, we compute the maximum likelihood planet mass from the probabilistic mass-radius relation forecaster (Chen & Kipping 2017) and analytically assess the Lagrange stability of each neighboring planet pair assuming circular orbits (Barnes & Greenberg 2006). Each planet’s scaled semimajor axis  $a/R_s$  and scaled radius  $r_p/R_s$  follow from their sampled radius  $r_p$  and the stellar parameters  $R_s$  and  $M_s$ . We sample impact parameters  $b$  from  $\mathcal{U}(0, 0.9)$  to compute the orbital inclinations. Furthermore, we adopt fixed quadratic limb darkening coefficients by interpolating the *Kepler* bandpass coefficient grid along  $T_{\text{eff}}$ ,  $\log g$ , and  $[\text{Fe}/\text{H}]$ , assuming solar metallicity when  $[\text{Fe}/\text{H}]$  measurements are absent (Claret et al. 2012). These parameters are used to compute transit models in the absence of any transit timing variations. Transit signals are then injected into the cleaned *K2* light curves and fed to ORION to conduct a blind search for transiting signals.

The detection sensitivity as a function of S/N for each *K2* star is computed by considering a minimum of  $10^2$  injected planetary systems per star and computing the recovery fraction of injected small planets with  $P \leq 100$  days. The average *K2* detection sensitivity curve, along with the 16<sup>th</sup> and 84<sup>th</sup> percentiles, are also included in Fig. 5. The quality of the pointing corrections within the EVEREST light curves can vary widely within our sample such that there is considerably more variance in the *K2* detection sensitivity relative to *Kepler*. Furthermore, the average detection sensitivity is significantly reduced compared to *Kepler*. The reduced sensitivity is due in-part to the imperfect corrections of the reduced pointing ac-

curacy and to the limited time baseline of  $\sim 80$  days in a typical *K2* light curve compared to *Kepler*. Furthermore, we have not attempted to optimize the performance of ORION on *K2* light curves beyond slight modifications to the algorithm's performance hyperparameters that were made to ensure the detection of 52/53? confirmed *K2* planets. The planet K2-21c (EPIC 206011691.02,  $P = 15.5$  days) remains undetected by ORION because of the algorithm's requirement to discard putative signals that are commensurate with other high S/N signals in the light curve. The presence of K2-21b at  $P = 9.32$  days is within 1% of a 5:3 period ratio with K2-21c and thus inhibits the identification of the 15.5 day signal as being independent and planetary.

#### 4.3. Two-dimensional sensitivity maps

The sensitivity curves depicted in Fig. 5 enable us to extend the visualization of the detection sensitivity to two dimensions. Explicitly, we consider the detection sensitivity  $s_{nij}$  for each star (indexed by  $n$ ) and as a function of  $P$  and  $r_p$  which are indexed by  $i$  and  $j$  respectively. Consideration of the sensitivity in the  $P$ - $r_p$  plane will be needed to evaluate the occurrence rates in that parameter space which is important for understanding the structure of the radius valley around low mass stars due to the dependence of the efficiency of atmospheric loss on both planet size and separation, regardless of the physical mechanism involved.

We consider orbital periods  $P \in [0.5, 100]$ ? days and planet radii  $r_p \in [0.5, 4]$   $R_\oplus$ . At each grid cell  $nij$  we compute the average S/N within the cell and map that value to the detection sensitivity using the data in Fig. 5. The detection sensitivity maps for *Kepler* and *K2*, averaged over the index  $n$ , are shown in Fig. 6.

#### 4.4. Survey Completeness

Only transiting planets are detectable in transit surveys. To correct for the non-detection of otherwise detectable but non-transiting planets we compute the geometric transit probability for each star  $n$  and at each grid cell  $ij$  in the  $P$ - $r_p$  space to be

$$p_{t,nij} = \frac{R_{s,n} + r_{p,j}}{a_{ni}}. \quad (5)$$

Note that we are only interested in the relative planet occurrence rate and therefore do not consider constant scalar modifications to  $p_{t,nij}$  from effects such as grazing transits or non-zero eccentricities (Barnes 2007).

The product of each star's detection sensitivity with its geometric transit probability yields completeness maps as a function of  $P$  and  $r_p$ . The average completeness maps for our *Kepler* and *K2* stars are shown in Fig. 7.

### 5. THE OCCURRENCE RATE OF SMALL CLOSE-IN PLANETS AROUND LOW MASS DWARF STARS

#### 5.1. Occurrence rates versus orbital period and planet radius

The detection and validation of planets from the *Kepler* and *K2* missions enable to measurement of the occurrence rate of planets given the completeness corrections derived in Sect. 4. For the index  $i$  representing a planet's orbital period and  $j$  representing the planetary radius, the probability of detecting an integer number

of planets within that grid cell ( $k_{ij}$ ) around  $N_s$  stars is given by the binomial likelihood function

$$\mathcal{L}_{nij}(k_{ij}|N_s, P_{nij}) = \binom{N_s}{k_{ij}} \prod_{n=1}^{N_s} P_{nij}^{k_{ij}} (1 - P_{nij})^{N_s - k_{ij}} \quad (6)$$

where

$$P_{nij} = s_{nij} \cdot p_{t,nij} \cdot f_{ij}, \quad (7)$$

is the probability of detecting a planet in the  $ij$  grid cell around the  $n^{\text{th}}$  star. This quantity is dependent on the detection sensitivity  $s_{nij}$ , the transit probability  $p_{t,nij}$ , and the intrinsic occurrence rate of planets in the grid cell  $ij$ :  $f_{ij}$ . The number of planet detections  $k_{ij}$  is depicted in Fig. 3 for  $i$  representing the orbital period and insolation. Together with our calculations of  $s_{nij}$  and  $p_{t,nij}$  for the  $N_s = 17393$  low mass stars in our sample (Figs. 6 and 7), and noting from Bayes theorem that the posterior probability of  $f_{ij}$  is

$$p(f_{ij}|N_s, s_{nij}, p_{t,nij}, k_{ij}) \propto \mathcal{L}_{nij}(k_{ij}|N_s, s_{nij}, p_{t,nij}, f_{ij}), \quad (8)$$

modulo the coefficient of proportionality which we set to unity.

Firstly, recall that there are  $\sim 5$  times more confirmed planets from *Kepler* than from *K2* in our sample (see Fig. 3) despite our sample having  $\sim 3.5$  times more *K2* stars (see Fig. 2). These factors compound to produce a lower planet occurrence rate measured with *K2* than with *Kepler* as the reduced *K2* detection completeness (see Fig. 7) is insufficient to account for the lower measured planet occurrence rates. The discrepancy instead arises from the disparate resources that have been dedicated to the confirmation of planets from *Kepler* and *K2*. The result being that the number of confirmed planets existing within the set of *K2* PCs is underestimated by the number of PCs that have been reported as validated so far. We address this discrepancy by scaling the cumulative occurrence rate measured by *K2* in our sample to that of *Kepler*. In this way, we are assuming that the planet populations studied by each mission are inherently identical despite existing within distinct stellar populations within the galaxy.

The maximum a-posteriori (MAP) map of  $f_{ij}$  is depicted in Fig. 8. The persistence of the radius valley from Sun-like to the low mass stars in our sample is clearly evident. Distinct peaks are separated along the planetary radius axis and span  $\sim 0.9 - 1.4 R_\oplus$  and  $\sim 1.9 - 2.3 R_\oplus$  respectively. Note however that the lower limit on the former peak nearly approaches the region in which the *Kepler* sensitivity falls below 10% and the  $f$  values become unreliable. The occurrence rates also highlight the relative dearth of planets larger than  $\sim 3 R_\oplus$  including the Neptunian desert at short orbital periods (Lundkvist et al. 2016; Mazeh et al. 2016). The large scale structure of the measured occurrence rates are also broadly consistent with previous investigations of the planet population around low mass *Kepler* stars (Dressing & Charbonneau 2013, 2015; Gaidos et al. 2016) such as the prominence of planets  $\lesssim 2 R_\oplus$  with  $P \sim 10 - 60$  days and a cumulative occurrence rate of 2.87? planets per star.

FIG. 6.— Average detection sensitivity versus orbital period and planetary radius. The detection sensitivity maps averaged over *Kepler* stars (*left panel*) and over *K2* stars (*right panel*) from our sample of low mass dwarf stars.

FIG. 7.— Average completeness versus orbital period and planetary radius. Maps of the product of the detection sensitivity and geometric transit probability averaged over *Kepler* stars (*left panel*) and over *K2* stars (*right panel*) from our sample of low mass dwarf stars.

FIG. 8.— Planet occurrence rate versus orbital period and planetary radius. The maximum a-posteriori occurrence rate map calculated from the population of confirmed planets from *Kepler* (circles) and *K2* (diamonds) around low mass dwarf stars. Overplotted are the empirical locations of the radius valley around FGK stars characterized via asteroseismology (*dashed line*, Van Eylen et al. 2018) and the approximate radius valley around early-M to mid-K dwarfs (*dotted line*, Wu 2019).

The location and slope of the radius valley (i.e.  $d \log r_p / d \log P$ ) are broadly consistent with the valley structure measured from the empirical planet population of FGK stars characterized via asteroseismology (Van Eylen et al. 2018). Wu (2019) also provided a visual approximation to the location of the radius valley around stars with  $M_s \in [0.5, 0.76] M_\odot$  in their *Gaia-Kepler* sample. However we find the location of the terrestrial-sized planet peak to exist at longer  $P \sim 30$  days compared to  $\sim 5$  days (c.f. Fig. 2, Wu 2019). The discrepancy likely stems from differences in the methods of correcting for survey incompleteness. Recall that in this study the detection sensitivity is computed for each star using its unique completeness products from the *Kepler* pipeline whereas Wu (2019) adopt piecewise completeness levels of 10, 50, or 90% complete as a function of  $P$  and  $r_p$  from Zhu et al. (2018).

Lastly, we note that the radius valley as a function of  $P$  does not appear to be completely void of planets. This may present evidence of the efficiency of the gap clearing mechanism around low mass stars and is discussed further in Sect. ??.

### 5.2. Occurrence rates versus planet radius

Next we marginalize over  $P$  and compute the one-dimensional occurrence rate of small, close-in planets as a function of  $r_p$ . The resulting occurrence rates are shown in Fig. 9 in which the bimodal distribution of planet sizes is again clearly discernible in the MAP occurrence rates. The uncertainties on each  $f_j$  bin are computed from the 16<sup>th</sup> and 84<sup>th</sup> percentiles of the  $f_j$  posterior. We ignore the occurrence rates in bins with  $r_p \lesssim 1 R_\oplus$  where our detection sensitivity is poor.

From the bimodal distribution we highlight the approximate radii likely corresponding to planets with terrestrial bulk compositions ( $r_p \lesssim 1.55 R_\oplus$ ) versus planets with significant size fractions in gaseous envelopes ( $r_p \gtrsim 1.55 R_\oplus$ ) around low mass stars. Also depicted in Fig. 9 is  $f_j$  with a binning scale twice that of the primary  $f_j$  depiction (i.e.  $0.06 R_\oplus$  compared to  $0.13 R_\oplus$ ). With this adopted fine binning the fractional uncertainties on  $f_j$  in each bin are sufficiently large to eliminate the significance of the distinct bimodal peaks. Despite this, the bimodality in the MAP occurrence rates continues to persist with the location of the valley features only being marginally affected. We interpret this as further evidence for the existence of the radius valley in the close-in planet population around low mass stars.

### 5.3. Inclusion of supplemental *K2* planet candidates

In an attempt to improve the counting statistics in the occurrence rate calculations, we consider an enlarged planet population. This population is the union of our

confirmed planet sample with a set of additional planet candidates (PCs) from the *K2* mission. Specifically, we consider the set of PCs reported by Kruse et al. (2019) from *K2* campaigns 0-8 that includes 126 PCs not already included in our sample of confirmed planets and orbiting stars contained within our stellar sample.

By definition, we cannot identify which PCs are true planets of interest for this study and which PCs are instead produced by an astrophysical false positive. The inclusion of *K2* PCs therefore requires that we account for sample contamination by false positives probabilistically. We do so by considering a number of studies from the literature that perform a transiting planet search in *K2*, from any subset of its campaigns, and present attempts at validating their uncovered PCs statistically based on follow-up observations (Montet et al. 2015; Crossfield et al. 2016; Dressing et al. 2017; Hirano et al. 2018; Livingston et al. 2018; Mayo et al. 2018). Each of these studies utilized some combination of ground-based photometry to validate planet ephemerides, reconnaissance spectroscopy to identify spectroscopic binaries, and speckle or AO-assisted imaging to search for nearby stellar companions to their PC host stars. Each of the aforementioned studies used their respective set of follow-up observations together with the statistical validation tool *vespa* (Morton 2012, 2015) to statistically classify their PCs as either a validated planet (VP)<sup>6</sup>, a false positive (FP), or some other inconclusive disposition (e.g. remains a PC). The FP rate around cool stars ( $T_{\text{eff}} < 4700$  K) from each study is estimated by calculating the ratio of the number of reported FPs to the total number of FPs and VPs. Notably, Crossfield et al. (2016) showed that the FP rate in their *K2* sample is dependent on the measured planet radius as giant PCs have a larger likelihood of being a FP. Hence, we focus on PCs with  $r_p < 4 R_\oplus$  when deriving FP rates.

The resulting FP rates are reported in Table 3. Half of the studies do not find any probable FP signals among the small PCs orbiting cool stars in their samples. In such cases only upper limits on the FP rate can be derived which all agree that the FP rate is  $\lesssim 20\%$  at 95%. The remaining studies each detect at least one FP such that a non-zero maximum likelihood FP rate is measured. Their average FP rate is 5.7% which is also in agreement with the derived upper limits from the aforementioned studies. We proceed by constructing  $10^3$  realizations of the planet population that includes confirmed planets from both *Kepler* and *K2* plus a subset of the 126 *K2* PCs from Kruse et al. (2019). The subset of included PCs are randomly sampled from the full PC set according to the adopted FP rate such that each realization

<sup>6</sup> We treat validated and confirmed planets as equivalent dispositions.



FIG. 9.— Occurrence rate of planets as a function of size. *Upper panel*: histogram depicting the relative occurrence rate of close-in planets with orbital periods  $< 100$  days derived from the population of confirmed *Kepler* and *K2* planets around low mass stars. The bimodal distribution of planet radii peaking at  $\sim 1$  and  $\sim 2.5$   $R_{\oplus}$  highlights the presence of the radius valley around low mass stars centered at  $\sim 1.5$   $R_{\oplus}$ . Uncertainties in the planet occurrences follow from binomial statistics and are limited by the relatively small number of confirmed planets around low mass stars from *Kepler* and *K2*. The measured occurrence rates below  $\sim 1$   $R_{\oplus}$  (shown in *grey*) should be ignored due to the poor detection sensitivity. *Lower panel*: identical occurrence rates as in the upper panel accompanied by the same occurrence rates with finer radius bins. The corresponding occurrence rate uncertainties are too large to robustly infer the presence of features but the bimodal structure continues to be exhibited in the maximum likelihood occurrence rates. The shaded regions highlight our approximate definitions of terrestrial planets ( $r_p \in [0.97, 1.57]$   $R_{\oplus}$ ), down to reasonable sensitivity limits, and gaseous planets ( $r_p > 1.57$   $R_{\oplus}$ ) around low mass stars. Note the outer limit of  $2.5$   $R_{\oplus}$  is arbitrary.

TABLE 3  
K2 FALSE POSITIVE RATES FOR SMALL PLANETS AROUND COOL STARS

Reference	$N_{FP}$	$N_{VP}$	FP rate [%]
Montet et al. (2015) <sup>a</sup>	0	8	$< 30.7$
Crossfield et al. (2016)	2	39	$4.9^{+6.0}_{-1.4}$
Dressing et al. (2017)	2	34	$5.6^{+6.4}_{-2.0}$
Hirano et al. (2018) <sup>a</sup>	0	16	$< 19.5$
Livingston et al. (2018) <sup>a</sup>	0	14	$< 21.0$
Mayo et al. (2018) <sup>b</sup>	1	14	$6.7^{+12.4}_{-2.0}$

NOTE. — Within each study we only consider PCs with  $r_p < 4$   $R_{\oplus}$  and orbiting cool stars with  $T_{\text{eff}} < 4700$  K. FP: false positive. VP: validated planet.

<sup>a</sup> These studies do not detect any FPs such that the reported FP rate upper limit is represented by its 95% confidence interval.

<sup>b</sup> Mayo et al. (2018) did not explicitly classify their non-validated planets as FPs so we define FPs within their sample as any PC whose false positive probability exceeds 10%.

contains  $0.943 \cdot 126 \approx 119$  PCs.

The effect of including PCs in the planet sample on the derived occurrence rates are compared to the results from only considering confirmed planets in Fig. 10. Again we scale the *K2* occurrence rates to those from *Kepler* such that the cumulative occurrence of close-in planets with  $r_p \leq 4$   $R_{\oplus}$  is identical between the two planet populations. The radius valley continues to be resolved in the MAP occurrence rates. Furthermore, the addition of PCs reduces the median  $f_j$  uncertainty among planets with  $r_p > 1$   $R_{\oplus}$  from 0.0216 to 0.0186 planets per star (i.e.  $\sim 15\%$  improvement). However, the partial filling of the gap is increased as the contrast between the maximum  $f_j$  of the terrestrial planet peak ( $r_p \sim 1.3$   $R_{\oplus}$ ) and the minimum  $f_j$  of the valley ( $r_p \sim 1.6$   $R_{\oplus}$ ) decreases from 0.070  $R_{\oplus}$  (3.2 $\sigma$ ) to 0.054 (2.9 $\sigma$ ).

## 6. EVOLUTION OF THE RADIUS VALLEY AROUND LOW MASS STARS

### 6.1. Slope of the radius valley

Fig. 11 shows the two-dimensional occurrence rate of close-in small planets in the  $F - r_p$  space. This depiction enables the comparison of the close-in planet population around low mass stars to the population around Sun-like stars (Fulton et al. 2017). It also enables the calculation of the slope of the radius valley with  $F$  which can then be compared to model predictions of the planet size marking the transition from terrestrial to gaseous planets versus insolation. We measure the slope of the valley by sampling planets from the inverse occurrence rates over the domains  $F \in [1, 30]$   $F_{\oplus}$  and  $r_p \in [1, 2.5]$   $R_{\oplus}$  such that the valley, where planets are less common in nature, dominate this synthetic population. The relative

number of sampled planets is then fit with a linear function in the  $\log F - r_p$  space depicted in Fig. 11. From  $10^3$  realizations of the resampled planet population we measure the average slope and its standard deviation to be  $dr_p/d \log F = -0.093 \pm 0.010$ . Similarly, in the  $P - r_p$  space we measure  $dr_p/d \log P = 0.191 \pm 0.011$ .

The negative slope  $dr_p/d \log F$  indicates that the location of the radius valley drops to smaller planet radii with increasing insolation (i.e. decreasing orbital period). This behavior is broadly consistent with models of the radius valley formation from the formation small terrestrial of bodies in a gas-poor environment (Lee et al. 2014; Lee & Chiang 2016; Lopez & Rice 2018). The theoretical scaling of the transition radius with insolation in the gas-poor formation scenario is  $r_{p,\text{valley}} \propto F^{-0.08}$  (Lopez & Rice 2018) which is consistent with our measured scaling of  $-0.093 \pm 0.010$ . This result is inconsistent with the models of photoevaporation and core-powered mass loss which each predict an increasing central valley radius with increasing insolation ( $r_{p,\text{valley}} \propto F^{0.11}$ ; Lopez & Rice 2018,  $r_{p,\text{valley}} \propto F^{0.10}$ ; Gupta & Schlichting 2019b).

The negative slope in the radius valley around low mass stars differs from the trend seen around Sun-like stars (Fulton et al. 2017). Fig. 11 compares the occurrence rates of small close-in planets around each stellar population. Multiple studies have concluded that the location of the radius valley around Sun-like stars drops to smaller planet sizes with decreasing insolation (e.g. Van Eylen et al. 2018; Martinez et al. 2019). Conversely, Fig. 11 indicates that the opposite may be true around low mass stars. This observational evidence may elucidate changes in the dominant physical mechanisms that sculpt the valley around different host spectral types.

### 6.2. Planet populations versus stellar mass

In addition to calculating the occurrence rates  $f_{ij}$  among our full stellar sample, we also consider the evolution of the planet population in unique host stellar mass bins. Fig. 12 shows the MAP  $f_{ij}$  maps in  $P - r_p$  space and the marginalized  $f_j$  distributions in four stellar mass bins: our full stellar sample ( $M_s \in [0.08, 0.90]$   $M_{\odot}$ ), the massive half of the sample ( $M_s > 0.63$   $M_{\odot}$ ), the low mass half of the sample ( $M_s < 0.63$   $M_{\odot}$ ), and a subset of the latter focusing on increasingly lower mass stars ( $M_s < 0.42$   $M_{\odot}$ ). The statistically significant resolution of the radius valley in the  $f_j$  occurrence rates is only accomplished with the full stellar sample. The reduction of the sample size in the three remaining mass bins inflates the  $f_j$  uncertainties such that the valley is seen at  $< 1\sigma$  and hence not detected. However, the characteristic bimodality is exhibited in the MAP  $f_{ij}$  of the full and massive half stellar samples. Furthermore, their  $f_{ij}$  structures are similar as the majority of our full planet sample orbit stars more massive than the median stellar



FIG. 10.— Comparison of occurrence rates with and without planet candidates included. *Left panel*: same as Fig. 9. *Right panel*: histogram depicting the relative occurrence rate of close-in planets with orbital periods  $< 100$  days derived from the population of confirmed planets from *Kepler* and *K2* and supplemented by 119 PCs around low mass stars from Kruse et al. (2019). The radius valley continues to be resolved with the inclusion of PCs which improve the median uncertainty on the occurrence rate bins although the gap becomes less prominent with numerous PCs partially filling the valley.

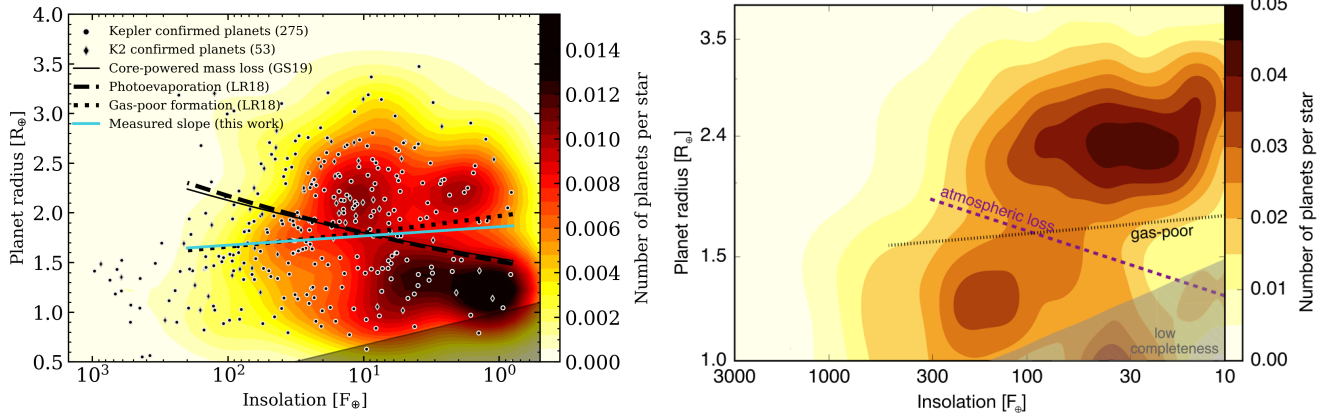


FIG. 11.— Planet occurrence rates versus insolation and planetary radius around low mass and Sun-like stars. *Right panel*: the maximum a-posteriori occurrence rate map calculated from the population of confirmed planets from *Kepler* (circles) and *K2* (diamonds) around low mass dwarf stars. Overplotted in black are model predictions of the transition from terrestrial to gaseous planets in the following scenarios: core-powered mass loss (Gupta & Schlichting 2019b), photoevaporation (Lopez & Rice 2018), and gas-poor formation Lopez & Rice (2018). We measure the slope of the radius valley to be  $dr_p/d \log F = -0.093 \pm 0.010$  which is broadly consistent with predictions from gas-poor formation of terrestrial planets.

TABLE 4  
RELATIVE OCCURRENCE RATES OF CLOSE-IN TERRESTRIAL  
AND GASEOUS PLANETS AROUND LOW MASS STARS

Stellar mass range [ $M_\odot$ ]	$f_{\text{terr}}$ $r_p \in [1, 1.6]$	$f_{\text{gas}}$ $r_p \in [1.6, 2.5]$	$f_{\text{terr}}/f_{\text{gas}}$
[0.08, 0.90]	$0.68 \pm 0.07$	$1.02 \pm 0.08$	$0.66 \pm 0.09$
[0.63, 0.90]	$0.69 \pm 0.11$	$1.28 \pm 0.16$	$0.54 \pm 0.11$
[0.08, 0.63]	$1.10 \pm 0.16$	$1.02 \pm 0.16$	$1.08 \pm 0.23$
[0.08, 0.42]	$1.64 \pm 0.43$	$0.19 \pm 0.09$	$8.46 \pm 4.62$

mass of  $0.63 M_\odot$  ( $\sim 62\%$ ).

In considering stars less massive than  $0.63 M_\odot$ , the gaseous planet peak begins to diminish relative to the terrestrial-sized planets. As evidenced in the MAP  $f_j$  distribution around stars with  $M_s \in [0.08, 0.63] M_\odot$ , the radius valley might persist around  $1.6 R_\oplus$  but the gaseous planet peak does not appear distinct from the terrestrial planet peak in the MAP  $f_{ij}$  map. That is that the relative frequency of terrestrial to gaseous planets appears to increase significantly around M dwarfs compared to the more massive K dwarfs. This feature is further accentuated around the lowest mass stars in our sample ( $< 0.42 M_\odot$ ) for which terrestrial-sized planets clearly dominate the distribution of close-in planets. The relative frequency of terrestrial to gaseous planets in each stellar bin are reported in Table ?? for fixed definitions of  $r_p \in [1, 1.6] R_\oplus$  and  $r_p \in [1.6, 2.5] R_\oplus$  respectively. The inner limit of  $1 R_\oplus$  restricts this analysis to where the detection sensitivity is still informative. The outer limit of  $2.5 R_\oplus$  is chosen such that the full width at half maximum of the gaseous planet peak in the  $f_j$  distribution from the full stellar sample (Fig. ??) is approximately identical for each peak.

The values in Table ?? indicate the significant increase in the relative occurrence of terrestrial planets with decreasing stellar mass that is also illustrated in Fig. ??. This is evidenced by our measurements show-

ing that gaseous planets are nearly twice as common as terrestrial planets around mid to late K dwarfs ( $M_s \in [0.63, 0.90] M_\odot$ ) while the relative frequency approaches unity around M dwarfs ( $M_s \in [0.08, 0.63] M_\odot$ ). Focusing on the lowest stellar mass bin considered, terrestrial planets become much more prominent as they outnumber gaseous planets by a factor of  $8.46 \pm 4.62$ . This result is broadly consistent the calculations of Hardegger-Ullman et al. (2019) who find that terrestrial-sized planets with  $r_p \in [0.5, 1.5] R_\oplus$  are about 4 – 5 times as common as gaseous planets ( $r_p > 1.5 R_\oplus$ ) around M3-5.5 dwarfs ( $M_s \in [0.12, 0.38] M_\odot$ ). Thus we have supporting evidence

### 6.3. Dependence of radius valley features on stellar mass

Here we measure the locations and uncertainties of features in the radius valley in each of the stellar mass bins considered in Sect. 6.2. In each of the four  $f_{ij}$  occurrence rate maps shown in Fig. 12, we measure the frequency-weighted central radius of the terrestrial planet peak, the gaseous planet peak, and the radius valley. We quantify the uncertainties in the feature locations by marginalizing over the following hyperparameters that can directly affect the inferred radius of each feature: the  $f_{ij}$  smoothing parameter, the minimum detection sensitivity, the  $P$  bin width, the  $r_p$  bin width, along with the imposed upper and lower  $P$  and  $r_p$  limits on each peak. These upper and lower  $r_p$  limits are defined based on the visual inspection of the  $f_{ij}$  maps in Fig. 12 and are used to demarcate the assumed boundaries of each peak, and by extension the valley separating the peaks. For example, if the boundaries on the terrestrial peak are set to 1-50 days and  $0.8$ - $1.4 R_\oplus$  then only the planet occurrence rates over that subset of the  $P - r_p$  parameter space are considered when calculated the  $f_j$ -weighted peak radius. The boundaries are listed in Table ?. In practice we de-

FIG. 12.— 2D and 1D planet occurrence rates in various stellar mass bins. *Top panels:* planet occurrence rate maps as a function of orbital period and planet radius. *Bottom panels:* distributions of the relative planet occurrence rate as a function of planet size. Note the differing occurrence rate scales. Each column corresponds to a unique cut in stellar masses which represent the full stellar sample ( $M_s \in [0.08, 0.93] M_\odot$ ), the early half of the stellar sample ( $M_s \in [0.63, 0.93] M_\odot$ ), the late half of the stellar sample ( $M_s \in [0.08, 0.63] M_\odot$ ), and the low mass bin ( $M_s \in [0.08, 0.42] M_\odot$ ) depicting a subset of the late half of the stellar sample. The relative occurrence of terrestrial to gaseous planets appears to increase around lower mass stars.

rive  $10^3$  realizations of each  $f_{ij}$  map with each realization having a unique set of hyperparameters. The resulting  $f_{ij}$  maps are marginalized over  $P$  and the  $f_j$ -weighted radius of each peak is computed over the domain bounded by the relevant hyperparameters (see Table ??). The same is done for the radius valley using the inverse occurrence rates.

The resulting locations of each radius peak and the valley are depicted in Fig. ?? as a function of stellar mass and given explicitly in Table ?. The depicted  $M_s$  values are given by the median and with uncertainties given by the 16<sup>th</sup> and 84<sup>th</sup> percentiles. In computing the feature locations we assume that the radius valley is present in all stellar mass bins despite the waning evidence for its existence around stars with  $M_s \lesssim 0.4 M_\odot$  (see Fig. 12). Our measured feature radii are compared to those measured in [Fulton & Petigura \(2018\)](#) around Sun-like stars with  $M_s < 0.97$ ,  $\in [0.97, 1.11]$ , and  $> 1.11 M_\odot$ . Most notably, the feature locations obtained from our full stellar sample continue to the trend of monotonically decreasing to smaller  $r_p$  with decreasing  $M_s$ . The slopes of this decrease for the terrestrial and gaseous planet peaks are  $dr_{p,\text{terr}}/dM_s = 0.40$  and  $dr_{p,\text{gas}}/dM_s = 0.97$  respectively indicating that the most common size of gaseous planet decreases more steeply with  $M_s$  than the typical size of terrestrial planets. We interpret this as being indicative of the effective disappearance of gaseous planets around increasingly lower mass stars (see Table ??). Furthermore, the reduced slope of the terrestrial peak may be indicative of a characteristic planetary core size of  $\approx 1 R_\oplus$ .

Models of the formation of the radius valley based upon photoevaporation ([Wu 2019](#)), gas-poor formation ([Lopez & Rice 2018](#)), and core-powered mass loss ([Gupta & Schlichting 2019b](#)) all make explicit predictions for the evolution of the radius valley location with stellar mass. Predictions from the core-powered mass loss scenario are dependent on the stellar mass-luminosity relation (MLR)  $L_s \propto M_s^\alpha$ . In Fig. 13, we consider cases with a constant MLR with  $\alpha = 5$  ([Gupta & Schlichting 2019b](#)) and with the empirically-derived piecewise MLR from [Eker et al. \(2018\)](#). All models predict a decreasing radius valley with decreasing stellar mass but differ in their slopes. At the median stellar mass of our full stellar sample ( $0.65 M_\odot$ ), the measured location of the radius valley is  $1.54 \pm 0.16 R_\oplus$ . This value favors a steep  $dr_p/dM_s$  slope although we are unable to distinguish between competing physical models given the uncertainty in the location. Fortunately, the model predictions continue to diverge with decreasing stellar mass. As such, measurements of the feature locations in decreasing  $M_s$  bins can be used to rule out the operation of certain physical mechanisms in the low stellar mass regime. Although the trend of decreasing median feature radii with decreasing stellar mass is upheld, the poor counting statistics in the reduced  $M_s$  bins prevent any significant inference regarding the relative strength of the competing physical mechanisms.

## 7. DISCUSSION & CONCLUSIONS

### 7.1. Improving constraints on the occurrence rate of small close-in planets orbiting mid-M dwarfs

The issue of having insufficient information to distinguish between photoevaporation, core-powered mass loss, and gas-poor formation around low mass stars can be addressed with two steps. Firstly, by expanding the low mass stellar sample in transiting searches for small close-in planets and secondly, by quantifying the detection sensitivity in those searches. NASA’s Transiting Exoplanet Survey Satellite (*TESS*; [Ricker et al. 2015](#)) will provide hundreds of new transiting planet discoveries in the vicinity of the radius valley ([Barclay et al. 2018](#)). *TESS* is particularly well-suited to the discovery of close-in planets around low mass stars down to M5V ( $M_s \sim 0.16 M_\odot$ ) due to its red bandpass (600-1000 nm) and its high cadence (2 minute) observations of 200,000-400,000 stars over  $\sim 94\%$  of the sky following its recently approved extended mission.

The *TESS* primary mission, lasting one year, has been ongoing since July 2018. Based on the mission’s performance at the time of writing, we can calculate the number of stars required to be observed by *TESS* to enable robust conclusions regarding the nature of the radius valley down to low mass stars. These calculations proceed by noting that based on binomial statistics, the measurement uncertainty on the feature locations scales as  $\sqrt{N_s P(1-P)}$  where  $N_s$  is the number of observed stars and  $P$  is the probability of detecting a small close-in planet given the detection sensitivity, its transit probability, and its inherent rate of occurrence (see Eq. 7). Through sectors 1-14, *TESS* has observed  $N_{s,\text{TESS}} = 23051$  stars less massive than  $0.4 M_\odot$  from its Candidate Target List (CTL; [Stassun et al. 2019](#)) with 2 minute cadence. Among these stars, the Science Processing Operations Center (SPOC; [Jenkins et al. 2016](#); [Twicken et al. 2018](#); [Li et al. 2018](#)) has reported ? objects of interest spanning the radius valley between  $1.4 - 1.6 R_\oplus$ . Assuming a 0% false positive rate among these planet candidates, this roughly implies a detection sensitivity of ? to transiting planets spanning the radius valley around stars with  $M_s < 0.4 M_\odot$ . Given the transit probability around those stars and assuming the same MAP occurrence rate of those planets from *Kepler* ( $f_{\text{valley}} \approx 0.19$  planets per star), we find that  $P_{\text{valley,TESS}} = ? \times 10^{-3}$ . We can compare these to the *Kepler* values of  $N_{s,\text{Kep}} = 33$  and  $P_{\text{valley,Kep}} = 4.513 \times 10^{-2}$  to scale the uncertainty on  $f_{\text{valley}}$ , and hence on the valley radius, as an increasing number of low mass stars are observed with *TESS*.

The resulting improvement in the measurement precision of the radius valley is shown in Fig. 14. ??

### 7.2. Implications for RV planet searches around low mass stars

Many existing and up-coming RV spectrographs will be partially focused on characterizing the masses of planets

TABLE 5  
ASSUMED BOUNDARY RANGES ON THE LOCATIONS OF RADIUS VALLEY FEATURES

Stellar mass range [M <sub>☉</sub> ]	log <i>P</i> lower boundary [days]	log <i>P</i> upper boundary [days]	Terrestrial peak lower <i>r<sub>p</sub></i> boundary [R <sub>⊕</sub> ]	Terrestrial peak upper <i>r<sub>p</sub></i> boundary [R <sub>⊕</sub> ]	Gaseous peak lower <i>r<sub>p</sub></i> boundary [R <sub>⊕</sub> ]	Gaseous peak upper <i>r<sub>p</sub></i> boundary [R <sub>⊕</sub> ]
[0.08, 0.90]	$\mathcal{U}(\log 0.5, \log 2)$	$\mathcal{U}(\log 50, \log 100)$	$\mathcal{U}(0.8, 1)$	$\mathcal{U}(1.2, 1.5)$	$\mathcal{U}(1.6, 1.9)$	$\mathcal{U}(2.3, 2.5)$
[0.63, 0.90]	$\mathcal{U}(\log 0.5, \log 2)$	$\mathcal{U}(\log 50, \log 100)$	$\mathcal{U}(0.8, 1)$	$\mathcal{U}(1.3, 1.5)$	$\mathcal{U}(1.8, 2)$	$\mathcal{U}(2.4, 2.7)$
[0.08, 0.63]	$\mathcal{U}(\log 0.5, \log 2)$	$\mathcal{U}(\log 50, \log 100)$	$\mathcal{U}(0.6, 0.9)$	$\mathcal{U}(1.2, 1.4)$	$\mathcal{U}(1.8, 2)$	$\mathcal{U}(2.1, 2.3)$
[0.08, 0.42]	$\mathcal{U}(\log 0.5, \log 2)$	$\mathcal{U}(\log 50, \log 100)$	$\mathcal{U}(0.5, 0.7)$	$\mathcal{U}(1.3, 1.4)$	$\mathcal{U}(1.7, 1.8)$	$\mathcal{U}(1.8, 2)$

NOTE. — The  $r_p$  boundaries on the radius valley are given implicitly by the upper  $r_p$  limit on the terrestrial peak and the lower  $r_p$  limit on the gaseous peak.

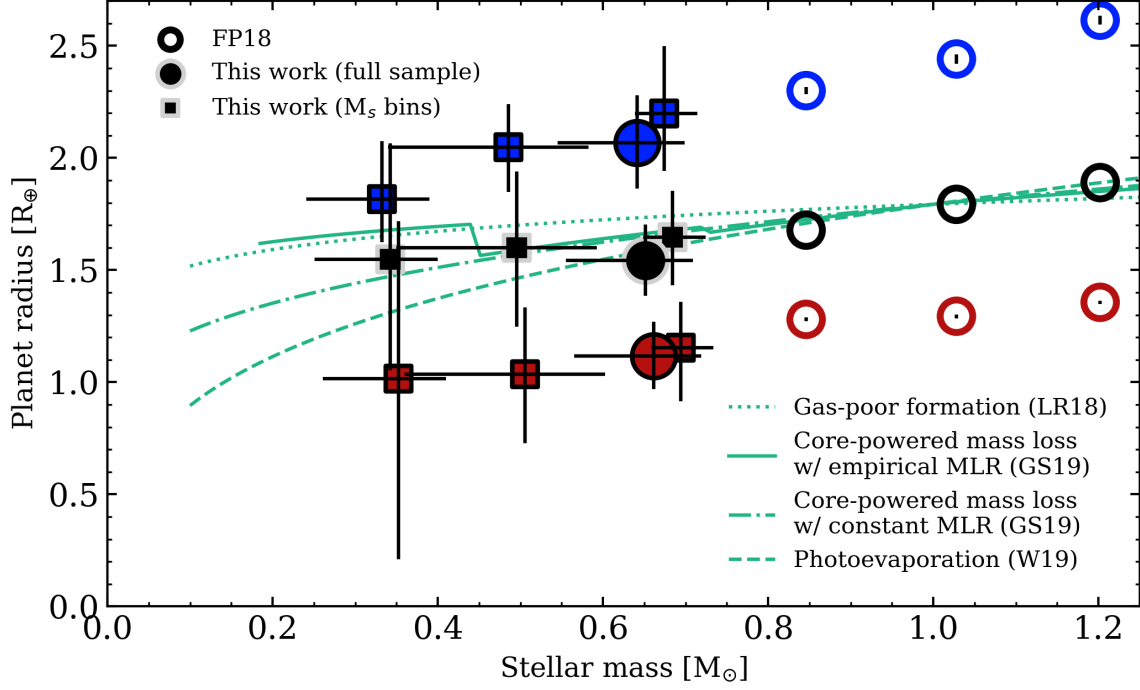


FIG. 13.— Evolution of the radius valley features with stellar mass. *Solid markers*: the occurrence rate-weighted locations of the terrestrial planet peak (*blue markers*), the radius valley (*green markers*) and the gaseous planet peak (*red markers*) as a function of host stellar mass for three  $M_s$  bins considered in this work:  $M_s \in [0, 0.8] M_\odot$ ,  $M_s \in [0.8, 1.0] M_\odot$ , and  $M_s \in [1.0, 1.2] M_\odot$ . The median stellar masses are depicted along with their uncertainties calculated from the 16<sup>th</sup> and 84<sup>th</sup> percentiles their respective stellar mass distribution. Uncertainties on the peak and valley locations are derived by sampling the measured occurrence rates and their uncertainties along with samples of the hyperparameters controlling map smoothing, minimum detection sensitivity, and the assumed feature ranges in planet radius. Similar measurements for Sun-like stars from [Fulton & Petigura \(2018\)](#) are plotted as *open markers*. The remaining curves represent theoretical predictions of the location of the radius valley based on models of atmospheric loss from core-powered luminosity with a constant mass-luminosity relation (*dashed*; [Gupta & Schlichting 2019b](#)), an empirical mass-luminosity relation (*dotted*; [Gupta & Schlichting 2019b](#)), and photoevaporation (*solid*; [Wu 2019](#)). The model curves are anchored at the valley location for  $M_s = M_\odot$ .

TABLE 6  
RADIUS VALLEY FEATURES VERSUS STELLAR MASS

Stellar mass [M <sub>☉</sub> ]	Terrestrial peak [R <sub>⊕</sub> ]	Radius valley [R <sub>⊕</sub> ]	Gaseous peak [R <sub>⊕</sub> ]
0.651 <sup>+0.058</sup> <sub>-0.096</sub>	1.118 <sup>+0.151</sup> <sub>-0.148</sub>	1.543 <sup>+0.160</sup> <sub>-0.160</sub>	2.068 <sup>+0.211</sup> <sub>-0.205</sub>
0.684 <sup>+0.040</sup> <sub>-0.035</sub>	1.154 <sup>+0.205</sup> <sub>-0.239</sub>	1.647 <sup>+0.207</sup> <sub>-0.215</sub>	2.197 <sup>+0.301</sup> <sub>-0.256</sub>
0.500 <sup>+0.097</sup> <sub>-0.146</sub>	1.036 <sup>+0.297</sup> <sub>-0.308</sub>	1.599 <sup>+0.340</sup> <sub>-0.352</sub>	2.048 <sup>+0.191</sup> <sub>-0.199</sub>
0.343 <sup>+0.057</sup> <sub>-0.092</sub>	1.017 <sup>+0.700</sup> <sub>-0.807</sub>	1.548 <sup>+0.515</sup> <sub>-0.496</sub>	1.815 <sup>+0.260</sup> <sub>-0.192</sub>

NOTE. — As depicted in Fig. 13.

spanning the radius valley in order to improve our physical understanding of the nature of those planets. The subset of those spectrographs operating in the near-IR, in particular, will focus heavily on M dwarf planetary sys-

FIG. 14.— Expected improvement in the measurement precision of the radius peak and valley locations with additional confirmed planets around stars with  $M_s \sim 0.3 M_\odot$ . Assuming a fixed detection probability (**dont do this**), the shaded regions depict the degree of improvement in the upper and lower limits on location of the super-Earth peak (*blue*), the radius valley (*green*), and the sub-Neptune peak (*red*) as additional planets are detected by missions like TESS. For stars with  $M_s \sim 0.3 M_\odot$ , model predictions of the valley location from photoevaporation and core-powered mass loss differ by  $\sim 0.4 R_\oplus$  (*dashed horizontal line*). Based on the performance of TESS to-date, the expected time to confirm such planets is parameterized as a linear function of time and is depicted on the secondary x-axis.

tems (e.g. CARMENES; [Quirrenbach et al. 2014](#), HPF; [Mahadevan et al. 2012](#), IRD; [Kotani et al. 2014](#), NIRPS; [Bouchy et al. 2017](#), SPIRou; [Donati et al. 2018](#)). In defining target samples that are equally complete on either side of the radius valley, it is critically important that



the transition location between terrestrial and gaseous planets is known. In our full stellar sample which includes mid to late K dwarfs, the measured radius valley location is  $1.54 \pm 0.16 R_{\oplus}$  although we remind the reader that the exact value is dependent on the planet's separation (see Fig. 11). A consistent value of  $1.55^{+0.52}_{-0.50}$  is also recovered, albeit with reduced significance, around stars later than about M2.5V. This value is slightly lower than the valley locations measured around Sun-like stars with  $M_s \sim 1.2 M_{\odot}$  of  $\sim 1.9 R_{\oplus}$  and  $M_s \sim 0.85 M_{\odot}$  of  $\sim 1.7 R_{\oplus}$  (Fulton & Petigura 2018).

This work elucidates the location of the radius valley around M dwarf host stars and guides observers to the planetary radii from transit surveys that are of interest for fully characterizing the radius valley in terms of planetary bulk densities.

mass dependence of the gap:

The weighted feature radii are also effected by planetary magnetic fields which directly impact the efficiency of atmospheric stripping in the photoevaporation scenario (?). The persistence of a planetary magnetic field acts to shield the planet's atmosphere from XUV stellar photons thus enhancing the retention of the atmosphere and shifting the location of the radius valley to larger radii.

valley filling increases with decreasing stellar mass

In the photoevaporation scenario, the partial filling of the gap around low mass stars may be explained by their lower XUV luminosities relative to Sun-like such as those included in the CKS stellar sample ().

This explanation seems to be supported by the stellar mass dependent gap measurements from Fulton & Petigura (2018).

summary of McDonald+2019 ([https://ui-adsabs.harvard.edu/abs/2019ApJ...876...22M/abstract](https://ui.adsabs.harvard.edu/abs/2019ApJ...876...22M/abstract)): X-rays only since XUV observations are difficult for non-Sun-like stars and X-rays are the dominant driver of atmospheric loss by photoevaporation. Jackson+12 & Shkolnik+14 derived scalings from data for the LX/Lbol evolution over time for 0.3 - 1.3 solar mass stars on the MS, low mass stars ( $\lesssim 0.8 M_{\odot}$ ) exhibit a LX/Lbol that is typically a few to ten times greater than around Sun-like stars ( $0.8 - 1.12 M_{\odot}$ ) (fig 1 in McDonald+2019). scaling these values by the typical bolometric luminosities of stars in the various mass bins reveals that Sun-like stars having higher absolute X-ray luminosities which contributes to more efficient clearing of the gap by photoevaporation.

hi

## REFERENCES

- Aigrain, S., Hodgkin, S. T., Irwin, M. J., Lewis, J. R., & Roberts, S. J. 2015, *MNRAS*, 447, 2880
- Aigrain, S., Parviainen, H., & Pope, B. J. S. 2016, *MNRAS*, 459, 2408
- Akeson, R. L., Chen, X., Ciardi, D., et al. 2013, *PASP*, 125, 989
- Bailer-Jones, C. A. L., Rybizki, J., Fouesneau, M., Mantelet, G., & Andrae, R. 2018, *AJ*, 156, 58
- Barclay, T., Pepper, J., & Quintana, E. V. 2018, *ArXiv e-prints*, arXiv:1804.05050
- Barnes, J. W. 2007, *PASP*, 119, 986
- Barnes, R., & Greenberg, R. 2006, *ApJL*, 647, L163
- Berger, T. A., Huber, D., Gaidos, E., & van Saders, J. L. 2018, *ApJ*, 866, 99
- Bouchy, F., Doyon, R., Artigau, É., et al. 2017, *The Messenger*, 169, 21
- Bovy, J., Rix, H.-W., Green, G. M., Schlafly, E. F., & Finkbeiner, D. P. 2016, *ApJ*, 818, 130
- Boyajian, T. S., von Braun, K., van Belle, G., et al. 2012, *ApJ*, 757, 112
- Burke, C. J., & Catanzarite, J. 2017, *Planet Detection Metrics: Per-Target Flux-Level Transit Injection Tests of TPS for Data Release 25*, Tech. rep.
- Burke, C. J., Christiansen, J. L., Mullally, F., et al. 2015, *ApJ*, 809, 8
- Chen, H., & Rogers, L. A. 2016, *ApJ*, 831, 180
- Chen, J., & Kipping, D. 2017, *ApJ*, 834, 17
- Choi, J., Dotter, A., Conroy, C., et al. 2016, *ApJ*, 823, 102
- Christiansen, J. L., Clarke, B. D., Burke, C. J., et al. 2015, *ApJ*, 810, 95
- . 2016, *ApJ*, 828, 99
- Christiansen, J. L., Vanderburg, A., Burt, J., et al. 2017, *AJ*, 154, 122
- Claret, A., Hauschildt, P. H., & Witte, S. 2012, *A&A*, 546, A14
- Cloutier, R. 2019, *AJ*, 158, 81
- Crossfield, I. J. M., Ciardi, D. R., Petigura, E. A., et al. 2016, *ApJS*, 226, 7
- Donati, J.-F., Kouach, D., Lacombe, M., et al. 2018, *SPIRou: A NIR Spectropolarimeter/High-Precision Velocimeter for the CFHT*, 107
- Dressing, C. D., & Charbonneau, D. 2013, *ApJ*, 767, 95
- . 2015, *ApJ*, 807, 45
- Dressing, C. D., Charbonneau, D., Dumusque, X., et al. 2015, *ApJ*, 800, 135
- Dressing, C. D., Vanderburg, A., Schlieder, J. E., et al. 2017, *AJ*, 154, 207
- Eker, Z., Bakış, V., Bilir, S., et al. 2018, *MNRAS*, 479, 5491
- Fressin, F., Torres, G., Charbonneau, D., et al. 2013, *ApJ*, 766, 81
- Fulton, B. J., & Petigura, E. A. 2018, *AJ*, 156, 264
- Fulton, B. J., Petigura, E. A., Howard, A. W., et al. 2017, *AJ*, 154, 109
- Gaidos, E., Mann, A. W., Kraus, A. L., & Ireland, M. 2016, *MNRAS*, 457, 2877
- Ginzburg, S., Schlichting, H. E., & Sari, R. 2018, *MNRAS*, 476, 759
- Gupta, A., & Schlichting, H. E. 2019a, *MNRAS*, 487, 24
- . 2019b, *arXiv e-prints*, arXiv:1907.03732
- Hardegree-Ullman, K. K., Cushing, M. C., Muirhead, P. S., & Christiansen, J. L. 2019, *AJ*, 158, 75
- Henry, T. J., & McCarthy, Jr., D. W. 1993, *AJ*, 106, 773
- Hirano, T., Dai, F., Gandolfi, D., et al. 2018, *AJ*, 155, 127
- Howard, A. W., Marcy, G. W., Bryson, S. T., et al. 2012, *ApJS*, 201, 15
- Howell, S. B., Sobeck, C., Haas, M., et al. 2014, *PASP*, 126, 398
- Huber, D., Zinn, J., Bojsen-Hansen, M., et al. 2017, *ApJ*, 844, 102
- Jenkins, J. M., Chandrasekaran, H., McCauliff, S. D., et al. 2010, in *SPIE, Vol. 7740, Software and Cyberinfrastructure for Astronomy*, 77400D
- Jenkins, J. M., Twicken, J. D., McCauliff, S., et al. 2016, in *SPIE, Vol. 9913, Software and Cyberinfrastructure for Astronomy IV*, 99133E
- Jin, S., & Mordasini, C. 2018, *ApJ*, 853, 163
- Jin, S., Mordasini, C., Parmentier, V., et al. 2014, *ApJ*, 795, 65
- Kotani, T., Tamura, M., Suto, H., et al. 2014, in *SPIE, Vol. 9147, Ground-based and Airborne Instrumentation for Astronomy V*, 914714
- Kreidberg, L. 2015, *PASP*, 127, 1161
- Kruse, E., Agol, E., Luger, R., & Foreman-Mackey, D. 2019, *ApJS*, 244, 11
- Lee, E. J., & Chiang, E. 2016, *ApJ*, 817, 90
- Lee, E. J., Chiang, E., & Ormel, C. W. 2014, *ApJ*, 797, 95
- Li, J., Tenenbaum, P., Twicken, J. D., et al. 2018, *arXiv e-prints*, arXiv:1812.00103

- Lindegren, L., Hernández, J., Bombrun, A., et al. 2018, *A&A*, 616, A2
- Livingston, J. H., Crossfield, I. J. M., Petigura, E. A., et al. 2018, *AJ*, 156, 277
- Lopez, E. D., & Fortney, J. J. 2014, *ApJ*, 792, 1
- Lopez, E. D., & Rice, K. 2018, *MNRAS*, 479, 5303
- Luger, R., Agol, E., Kruse, E., et al. 2016, *AJ*, 152, 100
- Luger, R., Kruse, E., Foreman-Mackey, D., Agol, E., & Saunders, N. 2018, *AJ*, 156, 99
- Lundkvist, M. S., Kjeldsen, H., Albrecht, S., et al. 2016, *Nature Communications*, 7, 11201
- Mahadevan, S., Ramsey, L., Bender, C., et al. 2012, in *SPIE*, Vol. 8446, *Ground-based and Airborne Instrumentation for Astronomy IV*, 84461S
- Mamajek, E. E., Torres, G., Prsa, A., et al. 2015, *arXiv e-prints*, [arXiv:1510.06262](https://arxiv.org/abs/1510.06262)
- Mandel, K., & Agol, E. 2002, *ApJL*, 580, L171
- Mann, A. W., Feiden, G. A., Gaidos, E., Boyajian, T., & von Braun, K. 2015, *ApJ*, 804, 64
- Martinez, C. F., Cunha, K., Ghezzi, L., & Smith, V. V. 2019, *ApJ*, 875, 29
- Mathur, S., Huber, D., Batalha, N. M., et al. 2017, *ApJS*, 229, 30
- Mayo, A. W., Vanderburg, A., Latham, D. W., et al. 2018, *AJ*, 155, 136
- Mazeh, T., Holczer, T., & Faigler, S. 2016, *A&A*, 589, A75
- Montet, B. T., Morton, T. D., Foreman-Mackey, D., et al. 2015, *ApJ*, 809, 25
- Morton, T. D. 2012, *ApJ*, 761, 6
- . 2015, *VESPA: False positive probabilities calculator*, *Astrophysics Source Code Library*, [ascl:1503.011](https://www.ascl.net/1503.011)
- Morton, T. D., & Swift, J. 2014, *ApJ*, 791, 10
- Owen, J. E., & Wu, Y. 2013, *ApJ*, 775, 105
- . 2017, *ApJ*, 847, 29
- Pecaut, M. J., & Mamajek, E. E. 2013, *ApJs*, 208, 9
- Petigura, E. A., Howard, A. W., & Marcy, G. W. 2013, *Proceedings of the National Academy of Science*, 110, 19273
- Petigura, E. A., Howard, A. W., Marcy, G. W., et al. 2017, *AJ*, 154, 107
- Petigura, E. A., Marcy, G. W., Winn, J. N., et al. 2018, *AJ*, 155, 89
- Quirrenbach, A., Amado, P. J., Caballero, J. A., et al. 2014, in *SPIE*, Vol. 9147, *Ground-based and Airborne Instrumentation for Astronomy V*, 91471F
- Ricker, G. R., Winn, J. N., Vanderspek, R., et al. 2015, *Journal of Astronomical Telescopes, Instruments, and Systems*, 1, 014003
- Rogers, L. A. 2015, *ApJ*, 801, 41
- Stassun, K. G., Oelkers, R. J., Paegert, M., et al. 2019, *AJ*, 158, 138
- Twicken, J. D., Catanzarite, J. H., Clarke, B. D., et al. 2018, *Publications of the Astronomical Society of the Pacific*, 130, 064502
- Van Eylen, V., Agentoft, C., Lundkvist, M. S., et al. 2018, *MNRAS*, 479, 4786
- Vanderburg, A., & Johnson, J. A. 2014, *PASP*, 126, 948
- Weiss, L. M., & Marcy, G. W. 2014, *ApJL*, 783, L6
- Wu, Y. 2019, *ApJ*, 874, 91
- Youdin, A. N. 2011, *ApJ*, 742, 38
- Zhu, W., Petrovich, C., Wu, Y., Dong, S., & Xie, J. 2018, *ApJ*, 860, 101